ACS Photonics

Article

pubs.acs.org/journal/apchd5

Fabrication of Split-Rings via Stretchable Colloidal Lithography

Yangjun Cai,[†,§] Yang Cao,[‡,§] Peter Nordlander,[‡] and Paul S. Cremer*[,†]

[†]Department of Chemistry, Pennsylvania State University, University Park, Pennsylvania 16802, United States

[‡]Department of Physics and Astronomy, Rice University, 6100 Main Street, Houston, Texas 77005, United States

Supporting Information

ABSTRACT: Herein, a facile new patterning method is demonstrated for creating pairs of split-ring resonators (SRRs) in a scalable manner over large surface areas. This method is based on a novel variation of colloidal lithography called stretchable colloidal lithography (SCL), which combines conventional colloidal lithography and stretchable poly(dimethylsiloxane) (PDMS) molds. To fabricate SRRs, arrays of circular polystyrene (PS) rings were fabricated by conventional colloidal lithography. The circular ring features could be transferred to a PDMS stamp, forming negative features, circular apertures on the stamp. The PDMS stamp was then stretched, thereby transforming the circular apertures into elliptical ones. By using the stretched PDMS molds for polymer imprinting, elliptical rings with nonuniform heights could be fabricated. Each elliptical ring could be transformed into a pair of PS SRRs by controlled O_2 reactive ion etching. Through a subsequent chemical wet etching step, PS SRRs could be readily transferred into an underlying gold film. The SRRs exhibited multiple modes of polarization-dependent plasmonic resonances in the visible and infrared spectral regions. Experiments and corresponding theoretical modeling demonstrated that these multiple resonances could be tuned in a predictable manner. All optical data compared well with results from electromagnetic simulations.

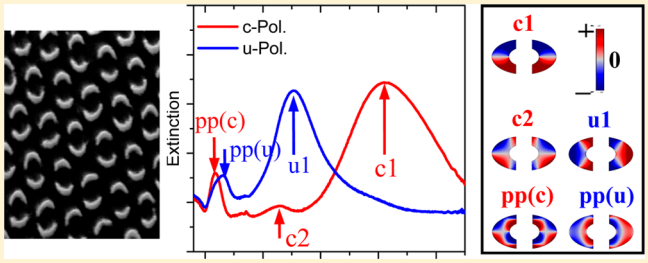

KEYWORDS: *split rings, colloidal lithography, gold, etch, surface plasmon resonance, poly(dimethylsiloxane)*

Metamaterials are artificially engineered structures with exotic properties that are not usually found in naturally occurring materials. Generally, they consist of periodic arrays of metallic structures with feature sizes less than the incident electromagnetic wavelength. Their optical and electronic properties are strongly dependent on the geometry of the unit structure rather than the constituent materials.[1] These architectures can manipulate electromagnetic waves in surprising ways and therefore exhibit several extraordinary properties, such as negative refraction[2] and coherent phenomena such as Fano resonances.[3] This opens up nascent but exciting potential applications, which affect a broad range of fields such as communications, lithography, data storage, light harvesting, and biomedical device fabrication.[4] Along with circular, square, and triangular shapes, split-ring resonators (SRRs) comprise some of the most common building blocks for metamaterials. Their ability to give rise to negative refractive indices (NRI) was first proposed by Pendry in 1999[5] and then experimentally demonstrated in 2001.[2] Over the past decade, SRRs have attracted extensive research interest and have found applications in sensors,[6,7] perfect lenses that beat the diffraction limit,[8] invisibility cloaks,[9,10] and photonic absorbers for photovotaics.[11,12]

A key challenge to realizing the widespread use of SRRs involves fabricating these structures over large areas (~cm^2). This is especially challenging for metamaterials operating in the infrared or visible range, which require nanometer-scale features. Conventional serial fabrication methods, such as electron beam lithography (EBL) and focused ion beam (FIB) milling cannot meet this requirement because these techniques normally only allow for sample fabrication over areas of 100 × 100 μm^2 or smaller. Indeed, trying to use EBL or FIB, to make nanosized SRRs over large areas results in low throughput and high costs. Alternatively, laser interference lithography and laser microlens array lithography also allows for fabricating large-area nanopatterns at high throughput.[13−15] However, both of these two methods require laser setup and precise alignment, respectively. Moreover, interference lithography only allows for the fabrication of standard periodic patterns, such as nanodots and gratings, and laser microlens array lithography requires the use of microlens with precise profiles. As such new efforts need to be put into the development of alternative fabrication methodologies.[16] So far, only a limited set of new approaches for large area/nanoscale fabrication have been developed. Such methods are usually based on colloidal lithography,[17−22] mechanical nanoskiving,[23,24] nanoimprinting lithography,[25] and capillary force lithography.[26] Among these, nanosphere lithography has particular promise for generating SRRs over large areas at high-throughput and low-cost.[17−21]

Recently, we developed a new variation of colloidal lithography, called stretchable colloidal lithography (SCL), to fabricate elliptically shaped rings in a scalable manner.[27] SCL

Received: November 18, 2013
Published: February 4, 2014

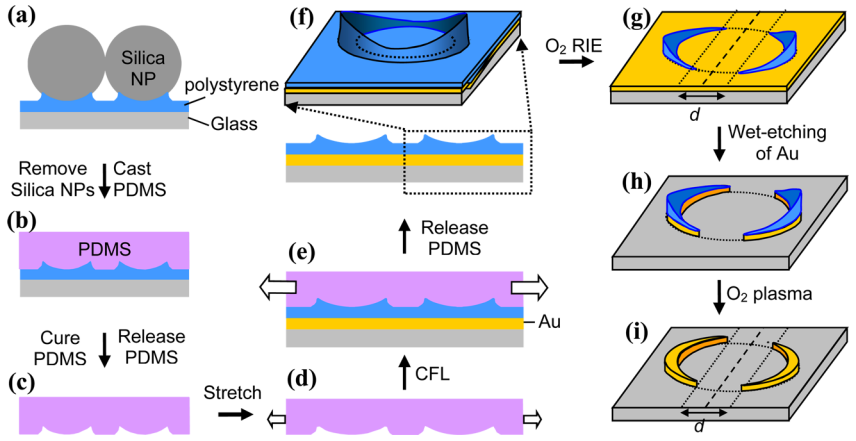

Figure 1. Schematic illustration of the procedure for fabricating Au SRRs.

overcomes a key limitation of conventional colloidal lithography, which otherwise allows for the fabrication of only circular geometries. In this new method, circular polymeric rings are first fabricated by using silica particles as templates, and their morphology is subsequently transferred to stretchable poly(dimethylsiloxane) (PDMS) molds. When the PDMS molds are stretched, the circularly imprinted ring patterns become transformed into ellipses, which can be used as molds for generating polymeric and metallic elliptical rings (ERs).[27] Herein, we demonstrate that these polymeric ERs can also be exploited to generate SRRs (Figure 1). The geometries and sizes of the SRRs can be readily tuned by varying the etching conditions. As such, the plasmonic resonance of these structures could be tuned in a quantitative manner.

EXPERIMENTAL SECTION

Materials. Glass slides (No. 2, 2 × 2 cm^2) were purchased from VWR. Polished Pyrex 7740 wafers (2.54 × 2.54 cm^2 and 0.5 mm thick) were obtained from Precision Glass and Optics (Santa Ana, CA). Aqueous suspensions of silica particles (1 μm in diameter) were purchased from Fisher Scientific. Polydimethylsiloxane (PDMS, Sylgard 184) and curing agent were obtained from Dow Corning. Polystyrene (PS) with a molecular weight (M_w) of 97000 was purchased from Scientific Polymer Products, Inc. (Ontario, NY). $Fe(NO_3)_3 \cdot 9H_2O$ and thiourea were procured of Fluka.

Fabrication of Rings. Figure 1 shows a schematic diagram of the procedure for generating SRR pairs. First, a PDMS stamp with circular apertures was made by SCL as previously described.[27] This was accomplished by first introducing a dispersion of silica particles onto a PS film on a glass slide (1.5 × 1.5 cm^2), which was pretreated with an O_2 plasma (HARRICK PDC-32G, 18 W for ~30 s, 200 mTorr of O_2). The O_2 plasma treatment rendered the PS film hydrophilic and therefore resulted in ordered arrays of assembled particles. Upon drying, the samples were annealed at 130 °C (above the transition temperature of PS: T_g ~ 100 °C) for 10 min to form circular PS rings (Figure 1a and Figure S1 in the Supporting Information). After removal of the silica particles by sonication, the circular PS ring patterns were transferred onto a PDMS stamp by casting PDMS on the substrate and subsequently curing at 70 °C for 6 h (Figure 1b). The PDMS stamp (1 mm in thickness) was released from the substrate (Figure 1c) and then stretched, thereby transforming the circular apertures into elliptical ones (Figure 1d). Subsequently, the stretched PDMS mold was put into conformal contact with a PS film on a Au/Cr (50 nm/5 nm) coated Pyrex glass wafer (~1.2 × 1.2 cm^2) and annealed at ~130 °C for 10 min (Figure 1e). After releasing the PDMS stamp, boat-like PS ERs of nonuniform height were formed on the PS film (Figure 1f). Next, the samples were treated by reactive ion etching (RIE) with oxygen (60 W, 250 mTorr, 20 sccm O_2; Figure 1g) and subsequent wet etching of gold (Figure 1h) and O_2 plasma (Figure 1i).

Characterization. The PS film thickness spin-coated on the Au layer and the residual film thickness after the formation of PS ERs was determined by measuring the depth of a scratch using atomic force microscopy (AFM). AFM was carried out with a Nanoscope IIIa Multimode scanning probe microscope (Veeco-Digital Instrumentals) in tapping mode. The PS ring structures and the Au rings were examined by AFM and scanning electron microscopy (SEM, JEOL JSM-7500F). Optical spectra of the Au elliptical rings on glass substrates were measured with a UV−vis-NIR spectrophotometer (Hitachi U-4100) at normal incidence in transmission mode over a wavelength range of 400−3000 nm. In order to investigate the effect of polarization, two polarizers were inserted into the light path before the sample and the reference.

Simulations. Commercial software (COMSOL Multiphysics 4.2) based on the finite element method has been used to numerically calculate the optical properties of SRRs. A pair of SRRs is modeled over the calculated region. The far-field transform boundary has been employed to obtain the scattering cross section. Perfectly matched layer (PML) was applied so that reflections would not go back into the simulated region. The plots of charge distribution density were generated by using Gauss's Theorem at the surfaces of the structures. Johnson and Christy's dielectric function for gold films[28] has been used for all simulations.

RESULTS AND DISCUSSION

Fabrication of SRRs. In our previous work, elliptical-shaped PS rings (PS ERs) were fabricated through similar procedures as shown in Figure 1a−f, in which the residual PS film was etched away and the remaining closed PS rings were utilized as wet-etching resists for generating elliptical Au rings.[27] To create SRRs, we began with the elliptically shaped PS rings developed in Figure 1f. Here we extended the RIE time and therefore not only the residual PS film but also part of the PS ERs were etched, as shown in Figure 1g. Due to the nonuniform height of the PS ERs, the closed ERs split upon

dx.doi.org/10.1021/ph400127g | ACS Photonics 2014, 1, 127−134

sufficient etching time along the short axis of the ERs, thereby forming pairs of PS SRRs on the gold film (Figure 1g). This step was followed by chemical wet etching of the gold film by using an aqueous solution of $Fe(NO_3)_3{\cdot}9H_2O$ (20 mM) and thiourea (30 mM), adjusted to pH 2.0 by HCl. Here, PS SRRs acted as etch masks, and the gold film was etched in the regions that were not covered by the PS (Figure 1h). Finally, the remaining PS was removed by O_2 plasma treatment and pairs of Au SRRs were left behind on the glass substrate (Figure 1i).

It should be noted that once a PDMS mold with circular apertures (Figure 1d) was fabricated, it could be used repeatedly to create SRRs. In our experiments, we have used it for up to 30 times with no noticeable degradation in pattern quality. This not only avoids the repeated fabrication of the PDMS mold, but also enhances the repeatability as replication from the same PDMS mold results in highly repeatable PS ERs (Figure 1f). One of the key steps in our fabrication procedure is the stretching of the PDMS stamp (Figure 1d), which was replicated from circular PS rings (see Supporting Information for the corresponding SEM images). The replicated PDMS stamp has ordered arrays of circular apertures, which contain depressed circular rings (Figure 2a). The corresponding AFM line profile reveals that the aperture depth is uniform along the perimeter ($h_0 \sim 36$ nm; Figure 2c). Upon stretching the PDMS stamp, the apertures exhibit two significant changes. First, these circular apertures were transformed into elliptical ones as illustrated schematically in Figure 2e. This is confirmed by the AFM scan of the PDMS stamp in the stretched state (Figure 2b).

Upon stretching, the diameter of the circular apertures, D_0, increased to D_L in the direction parallel to the applied stress ($\sigma_L = (1 + \varepsilon)E$, where ε and E are the strain and Young's modulus of PDMS, respectively (Figure 2e). However, the width in the direction perpendicular to the applied stress decreased to D_S (Figure 2e). Such a decrease was caused by Poisson contraction stress, ($\sigma_S = (1 - 0.5\varepsilon)E$). Second, the depth of the apertures also changed upon stretching. As can be seen from the line profiles of the elliptical apertures (Figure 2d), while the depth at the two ends along the long axis ($h_L \sim 38$ nm) was close to h_0 (~36 nm), the depth along the short axis (h_S ~24 nm) was shorter than h_0. In other words, when circular apertures are stretched, the apertures for long axes are expanded and maintain the original depth (left panel in Figure 2f); however, the apertures along the short axes are contracted by a Poisson contraction stress, leading to a partial collapse at the bottom of the apertures (right panel in Figure 2f).

With the nonuniform depth, the polymer structures imprinted from the stretched PDMS stamp exhibit similar nonuniform geometries as shown in Figure 3a. Specifically, it is lowest along the short axis (green dotted line) and highest along the long axes (blue dotted line), leading to boat-like structures. A line profile from the AFM image quantifies the profile of these boat-like structures, where the two ends of the ER along the long axis are ~25 nm higher than those along the short axis (Figure 3b). Here the height difference in PS ERs is slightly smaller than the depth difference of the PDMS apertures (i.e., $h_L - h_S$), which could be caused by an AFM artifact in measuring deep apertures.

As demonstrated above, Au SRRs can be fabricated by exploiting the nonuniform height of PS ERs, whereby the latter is partially etched away. The height difference ($h_L - h_S$) of PS ERs between the two axes is the key to the formation of SRRs by subsequent controlled etching. In order to split the closed ER in the RIE process, the height along the short axis needs to be smaller than that along the long axis. Figure S2 shows the values of h_L and h_S for the ERs of different aspect ratios (AR = 1.0–2.1), which were fabricated by applying different stresses. Here, AR is defined as the ratio of the outer diameter along the long axis to that of the outer diameter along the short axis (i.e., D_L/D_S). It was found that while the height along long axes (h_L) remained almost constant (~55 nm), the height along short axes (h_S) decreased with increasing AR up to 1.5 and then

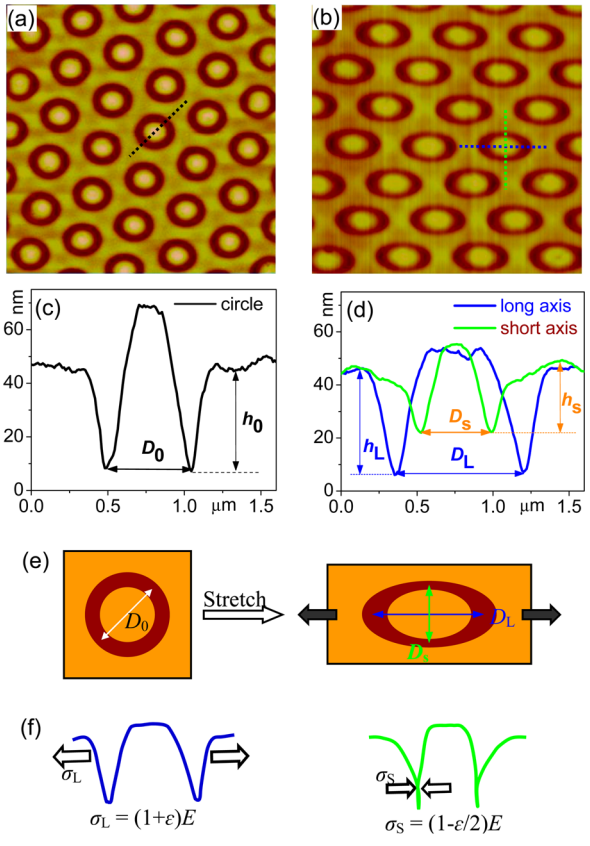

Figure 2. AFM images (5 × 5 μm^2) of the PDMS stamp replicated from circular PS rings generated from colloidal lithography (a) before and (b) after stretching (stain ~40%), respectively. (c, d) Corresponding line profiles from (a) and (b), respectively. (e) Schematic illustration of the geometrical transformation from circular to elliptical apertures upon stretching. (f) Schematic illustration of the stretch (left) and collapse (right) of PDMS apertures under the external stress (σ_L) and the induced Poisson contraction stress (σ_S), respectively.

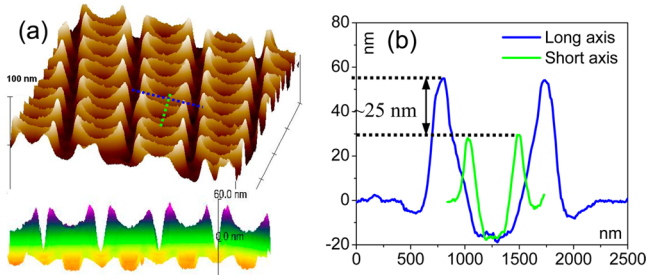

Figure 3. (a) 3-D (top) and side-view (bottom) AFM images (5 × 5 μm^2) of the PS ERs. (b) Line profiles of PS ERs along the long and short axes as indicated in (b).

dx.doi.org/10.1021/ph400127g | ACS Photonics 2014, 1, 127–134

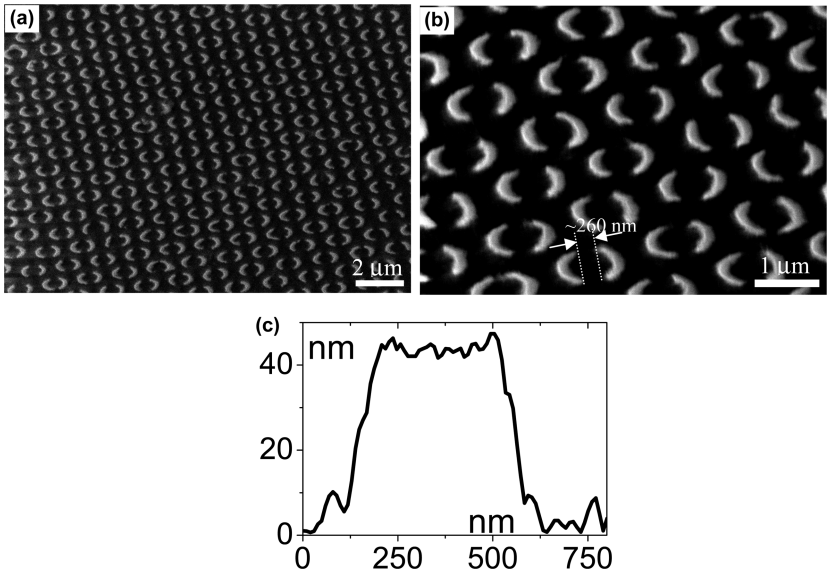

Figure 4. (a) Low and (b) high magnification SEM images of pairs of SRRs on a glass substrate. The average gap distance of the SRRs is ~260 nm. (c) AFM line profile shows that the height of the SRRs is around 45 nm.

leveled off. As such, when the AR was 1.0 or 1.2, h_L was too close to h_S, which is not suitable for SRR fabrication. When the AR was above 1.2 (e.g., AR =1.5), the height difference, $h_L - h_S$, increases to 20 nm, which was large enough to split the closed ring through controlled RIE.

We used the PS ERs in Figure 3, which had an AR of ~1.8 and a height difference of 25 nm, for the fabrication of SRRs. After RIE and wet chemical etching, ordered arrays of Au SRR pairs were obtained on the glass substrate as demonstrated by low and high magnification SEM images, Figure 4a and b, respectively. In this case, the generated SRRs have a separation distance (d) between two split ends of 260 ± 55 nm (Figure 4b). The height of the Au SRRs are uniform, as expected (~45 nm thick), as evidenced by the AFM line profile shown in Figure 4c.

Control of the Geometries of SRRs. The method described above allows for a high degree of feature tunability by varying the size of the silica particles, the annealing time/temperature, the conditions of RIE and the duration of the chemical wet etching step.[29,30] Moreover, the AR can be readily tuned by modulating the applied stress,[27] resulting in different geometries for the SRRs. Below, we will demonstrate that the separation distance between two SRRs or the size of the SRRs can be easily tuned even after the formation of PS ERs.

As shown by the 3D AFM image in Figure 3a, the height of PS ERs gradually increases from a minimum value along the short axes to a maximum value along the long axes. Therefore, it should be possible to control the separation distance of SRR pairs simply by varying the RIE time. The height, $H(x)$, of the polymer ERs above the Au substrate can be treated as the sum of two parts, as illustrated in the inset of Figure 5a. First, there is a residual PS film above the gold surface in the flat regions of the surface, which has a constant thickness ($h_0 \sim 40$ nm). Second, there is an additional height, $h(x)$, of the PS elliptical rings above the residual film. $h(x)$ increases gradually as one moves from the minimum along the short axis to the maximum value along the long axis of the elliptical ring, as shown in the inset scheme in Figure 5a. As such, the overall height ($H(x) = h_0 + h(x)$) also increases with the distance (x) away from the center of the short axis (Figure 5a). Due to the symmetry of the

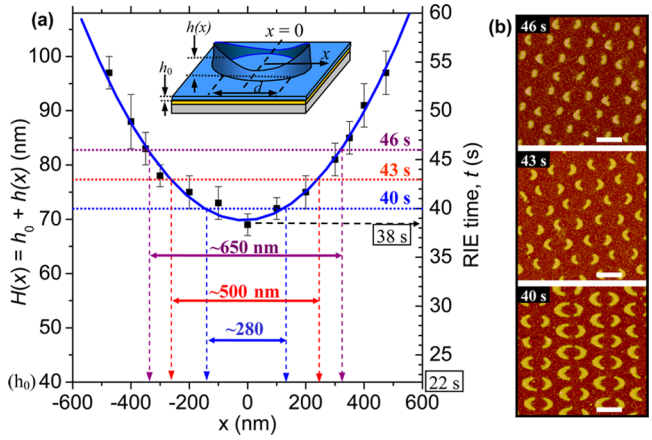

Figure 5. Control of the separation distance of SRR pairs. (a) Plot of the height of PS ERs ($H(x) = h_0 + h(x)$, left y-axis) and the corresponding O_2 RIE time (t, right y-axis) as a function of the distance (x) away from the center of the short axis. The inset schematic diagram shows the path for the distance (x), the separation distance (d), and the height of PS ERs (h_0 and $h(x)$). The value of H is the sum of the thickness of the residual PS film (h_0) and the PS ER above the residual film ($h(x)$), measured from the AFM images of the PS ERs (e.g., Figure 3a). The right y-axis is the time that is required to etch the corresponding PS thickness at the left y-axis based on the O_2 RIE rate ($v_{RIE} = H(x)/t \sim 1.8$ nm/s). (b) Three representative AFM images (5 × 5 μm^2, scale bars: 1 μm) of SRRs with separation distances of 627 ± 36, 520 ± 34, and 260 ± 55 nm generated at the RIE times of 40, 43, and 46 s, respectively.

ERs, $H(x)$ is approximately identical to $H(-x)$. Therefore, the resulting separation distance, d, approximately equals $2x$ (i.e., $d = 2x$; inset scheme of Figure 5a).

In Figure 5a, the left-hand y-axis indicates $H(x)$, while the right-hand y-axis shows the RIE time (t) needed to remove that corresponding height of the PS film from the surface. The RIE etching rate, $H(x)/t$, is approximately 1.8 nm/s, which can be discerned by noting that the RIE time needed to remove the residual film ($h_0 \sim 40$ nm) is ~22 s (x-axis in Figure 5a). This time should also represent an absolute lower bound for the time needed to fabricate ERs. In practice, it was found that the

dx.doi.org/10.1021/ph400127g | ACS Photonics 2014, 1, 127−134

minimum RIE time for obtaining Au SRRs was ~38 s (horizontal black dash line in Figure 5a). Furthermore, when the etching time was increased (40, 43, to 46 s), the separation distance (d) should correspondingly increase to 280, 500, and 650 nm, respectively (see blue, red, and purple arrows in Figure 5a). These values are obtained by simply noting the thickness along the elliptical rings which needed to be etched away at each RIE time. Indeed, such predicted values agree very well with the experimentally measured values (260 ± 55, 520 ± 34, and 627 ± 36 nm) from the AFM images in Figure 5b. Thus, the etch rate can be used to predict the split ring separation distance.

Optical Spectra of SRRs. After fabrication, the SRRs were characterized by UV−vis-NIR measurements (400−3300 nm) at the normal incidence. Figure 6a shows the extinction spectra,

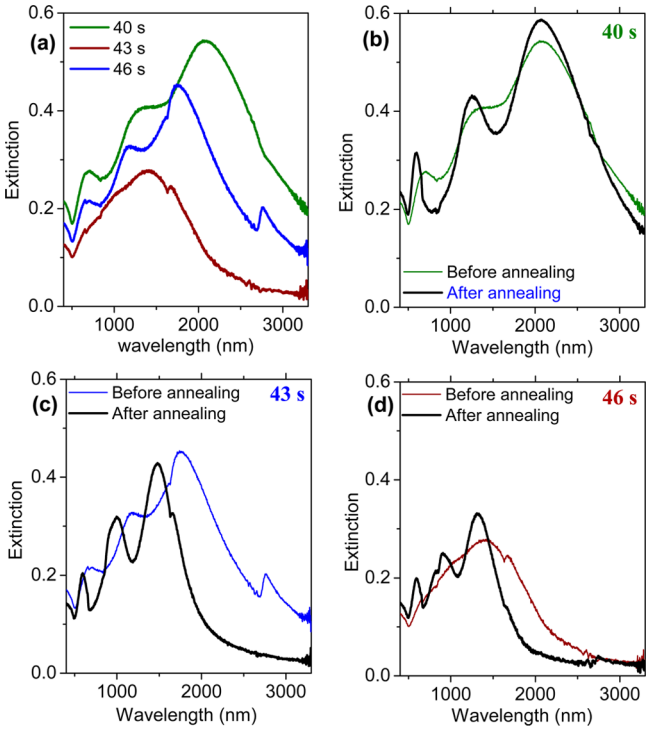

Figure 6. Effect of thermal annealing on the optical spectra of SRRs. (a) Extinction spectra of the as-fabricated SRRs (before thermal annealing) obtained at O_2 RIE time of 40, 43, and 46 s. (b−d) Comparison of the extinction spectra of the SRRs obtained at different RIE times before (green, blue, and maroon lines) and after (black line) annealing.

measured with unpolarized light, for the three SRR pairs from Figure 5b. As can be seen, the spectra exhibited broad LSPR peaks that became less pronounced and even broader as the distance between SRR pairs increased. Much of the broadening in these cases should be caused by the nonuniformity in sizes of the SRR features as well as the roughness induced during the fabrication process (e.g., chemical wet-etching). In order to improve the quality of the resonances, we thermally annealed the SRRs.[31,32] For gold, the melting temperature, T_m, is 1337 K (1064 °C)) and the temperature at which the atoms start to diffuse, known as the Tammann temperature ($T_T \sim 0.5T_m$), is 669 K (396 °C).[33] Therefore, the annealing temperature was set to 500 °C, which is well above T_T. After thermal annealing at 500 °C for 4 h, we found that the gold surface indeed became smoother (Figure S2 in Supporting Information).

Figure 6b−d shows the comparison of the extinction spectra of the three different SRRs before and after thermal annealing. For all three cases, the peaks sharpened substantially. Moreover, some of the resonant peaks were also blue-shifted, which is consistent with a slight contraction of the length of these particles as the edges are rounded.

Next, we investigated the origin of the plasmonic resonances of the SRRs. Figure 7a shows the extinction spectra of the SRRs

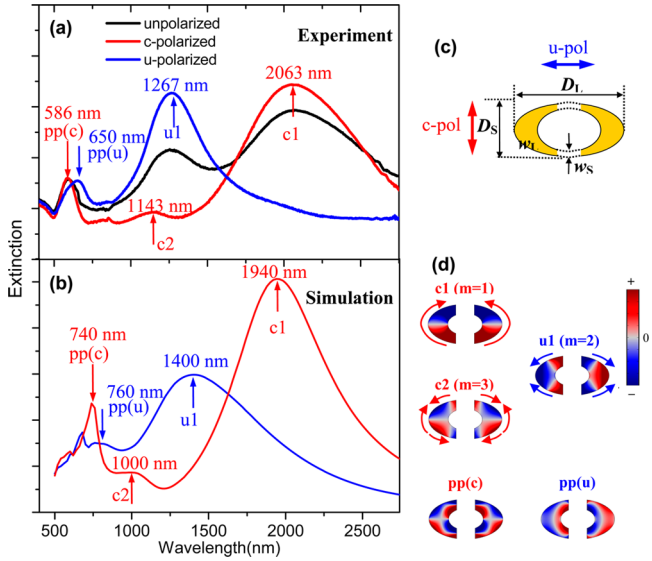

Figure 7. Experimental (a) and simulated (b) extinction spectra of Au SRRs. The black, red, and blue lines indicate unpolarized and c and u-polarized light, respectively. (c) Schematic diagram of SRRs showing the c- and u-polarizations and geometries used in simulation. (d) Simulated charge density distributions of different modes and polarizations. The red and blue arrows surrounding the charge density distributions show the instantaneous directions of the induced currents.

(O_2 RIE time of 40 s) upon illumination with both unpolarized and polarized light. In the following, we refer to the two polarizations as u- and c-polarizations, as defined in Figure 7c. For the c-polarization (c-pol, red line in Figure 7a), the extinction spectrum exhibited three main resonant peaks centered at 2063, 1143, and 586 nm. The strong resonance at 2063 nm, labeled c1, is associated with the plasmonic resonance along the contour of the C-shaped split ring. The weaker resonance at 1143 nm, labeled c2, is a higher-order mode resonance. The third peak, labeled pp(c), can be assigned to a resonance perpendicular to the SRR tips. This resonance is analogous to particle resonances observed in small gold nanoparticles or disks.[18,21,34] For the u-polarization (u-pol, blue line in Figure 7a), only a strong peak, termed u1, appears at 1267 nm in the spectrum. The highest energy peak for the u-polarization, labeled pp(u), is similarly associated with the resonance perpendicular to the contour of SRRs, which slightly red-shifted to 650 nm as compared to pp(c). Comparison between the spectra obtained from nonpolarized and polarized light indicates that the c1 and u1 resonances observed for nonpolarized light are in agreement with those observed with polarized light, but the weak c2 resonance overlapped with the u1 resonance in the nonpolarized spectrum.

In order to verify the above assignments of the resonances, the extinction spectra of an SRR pair were simulated by Comsol (Figure 7b). For these simulations, we used a pair of SRRs with

dx.doi.org/10.1021/ph400127g | ACS Photonics 2014, 1, 127−134

a gap distance (d) of 280 nm, which was obtained from an ER with D_L, D_S, w_L, and w_S of 1118, 607, 298, and 140 nm, respectively (see definitions of parameters in Figure 7c). It is observed that all resonances assigned in experiments (Figure 7a) are also present in the simulation and the wavelengths of the corresponding resonances agree well with each other. The simulated charge density distributions of the corresponding resonances are shown in Figure 7d. In the density distribution plots, red and blue represent two opposite charges (i.e., +ve and −ve) and white represents the standing wave node (neutral point). These charge distributions define induced currents in SRRs (arrows surrounding the charge distributions in Figure 7d) and the order of the standing waves oscillating in the SRRs. The orders of the modes are defined by the number of nodes (i.e., the white strips in Figure 7d) in the charge density distributions. For the c1 mode (1940 nm), there is one node in each SRR, indicating a dipolar resonance with a mode number of m = 1. Similarly, because the u1 (1400 nm) and c2 (1000 nm) modes have two and three nodes, respectively, their mode number should be m = 2 and m = 3, as indicated in Figure 7d. In addition, the charge distributions of the pp(c) (740 nm) and pp(u) (760 nm) modes confirm that the resonances are the result of polarizations of SRRs perpendicular to the two tips and the contour of the SRRs, respectively.

In order to investigate the tunability of resonances by the RIE time, the extinction spectra of the SRRs fabricated at three different O_2 RIE times (40, 43, and 46 s) are plotted in Figure 8a. It is clear that resonances of the same polarization and mode

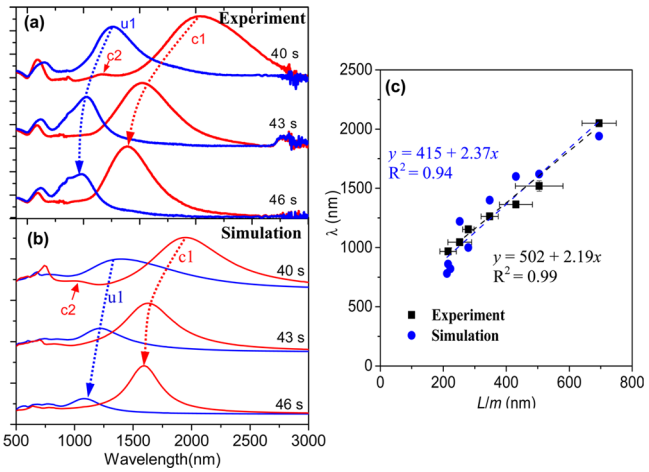

Figure 8. (a, b) Experimental and simulated extinction spectra of arrays of SRR pairs generated at different O_2 RIE times (40, 43, and 46 s), as shown in Figure 5b, respectively. In (a) and (b), the red and blue lines indicate c- and u-polarizations, respectively. The red and blue dotted arrows are used to indicate the changes of the resonant wavelengths of the same polarization and mode. (c) Plots of experimental (black) and simulated (blue) resonance wavelengths (λ) as a function of L/m. The dash lines are linear fits.

generally blue-shift and decrease in intensity with increasing RIE time (see the dotted arrows in Figure 8a). For all three cases, the wavelengths of the pp(c) resonances are slightly larger than those of pp(u) resonances. While the pp(c) resonances remain almost fixed at ∼586 nm, the pp(u) resonances do slightly blue-shift with decreasing SRR size. In addition, the c2 resonance is only observed for the largest SRRs. To further analyze the experimental results, we simulated the extinction spectra for pairs of SRRs for all cases (Figure 8b). Clearly, all resonances (c1, u1, and c2) exhibited the same trends observed in the experimental data. Specifically, the same blue-shifts and decrease in peak size can be observed with the increase of etching time (dotted arrows in Figure 8b).

In order to further understand the microscopic origin of the SSR resonances, we employed a simple standing-wave model for their wavelengths λ:

$$L = \frac{m(\lambda + \lambda_0)}{2n_{\text{eff}}} \Leftrightarrow \lambda = 2n_{\text{eff}}\left(\frac{L}{m}\right) - \lambda_0 \quad (1)$$

where L is the contour length of the SRR, m is the mode index of each resonance, n_{eff} is the effective refractive index of the surrounding medium, and λ_0 is a constant that depends on the geometric structure.[35,36] We plotted the measured and calculated λ value as a function of L/m in Figure 8c. As can be seen, the relationship between these variables is linear for both the experimental and simulated data. This suggests that the standing wave model with its linear relationship between λ and L/m can qualitatively explain the tunability of the SRR resonances. The slope obtained from eq 1 is $2n_{\text{eff}}$. In the present experiment, with the SRRs surrounded by air and the glass substrate, n_{eff} can be approximated as

$$n_{\text{eff}} = \sqrt{\frac{n_A^2 + n_S^2}{2}} \quad (2)$$

where n_A and n_S are the refractive indices of the air (n_A = 1) and the glass substrate (n_S = 1.47),[23,37] respectively. This leads to an n_{eff} of 1.26. Based on the linear fittings in Figure 8c, the n_{eff} values are 1.10 and 1.19 for experiments and simulation, respectively. Although these data are slightly smaller than estimated values, they are in reasonable agreement (i.e., 1.0 < n_{eff} < 1.47). Here the slight difference between the experiments and simulations can be attributed to the uncertainty in n_{eff}. In the simulations, we used the value estimated from eq 2 where it is assumed that the coverage of the gold feature by the glass substrate (n_S = 1.47) and air (n_S = 1.0) are the same (∼50%). In the experiments, however, the coverage of the glass substrate should be somewhat less because the vertical walls of the gold SRRs are also covered by air, which would results in a smaller n_{eff}.

CONCLUSION

We have demonstrated a new method for generating pairs of SRRs by the combination of colloidal lithography and mechanical stretching. A pair of SRRs can be obtained from each colloidal particle. The geometries of the SRRs, including the size and separation distance, could be qualitatively controlled by simply varying the RIE time. Arrays of the SRRs gave rise to multiple polarization-dependent resonances ranging in frequency from the visible to NIR. Both the experimental and simulation data indicated that the tunability of the resonances could be explained by a standing wave model, which also provides a simple method to predict the wavelengths of the SSR resonances. As our method is based on colloidal lithography and allows for large-scale fabrication, the fabricated structures can provide versatile platforms for plasmonic sensor design and metamaterials.

ASSOCIATED CONTENT

Supporting Information

SEM images of circular polymer rings; height of PS ERs above the residue PS films at the long (h_L) and short (h_S) axes with

dx.doi.org/10.1021/ph400127g | ACS Photonics 2014, 1, 127−134

different ARs; comparison of gold surfaces before and after thermal annealing. This material is available free of charge via the Internet at http://pubs.acs.org.

AUTHOR INFORMATION

Corresponding Author

*E-mail: psc11@psu.edu.

Author Contributions

§These authors contributed equally to this work (Y.C. and Y.C.).

Notes

The authors declare no competing financial interest.

ACKNOWLEDGMENTS

P.S.C and Y.C. thank the Norman Hackerman Advanced Research Project (NHARP, 010366-0040-2009) from the Texas Higher Education Coordinating Board and the Office of Naval Research (N00014-08-0467). We thank N. Large for helpful guidance on modeling calculations. P.N. and Y.C. were supported by the Robert A. Welch Foundation (C-1222) and the Office of Naval Research (N00014-10-1-0989).

REFERENCES

(1) Large, N.; Aizpurua, J.; Lin, V. K.; Teo, S. L.; Marty, R.; Tripathy, S.; Mlayah, A. Plasmonic Properties of Gold Ring-Disk Nano-Resonators: Fine Shape Details Matter. *Opt. Express* **2011**, *19*, 5587−5595.

(2) Shelby, R. A.; Smith, D. R.; Schultz, S. Experimental Verification of a Negative Index of Refraction. *Science* **2001**, *292*, 77−79.

(3) Luk'yanchuk, B.; Zheludev, N. I.; Maier, S. A.; Halas, N. J.; Nordlander, P.; Giessen, H.; Chong, C. T. The Fano Resonance in Plasmonic Nanostructures and Metamaterials. *Nat. Mater.* **2010**, *9*, 707−715.

(4) Zheludev, N. I. The Road Ahead for Metamaterials. *Science* **2010**, *328*, 582−583.

(5) Pendry, J. B.; Holden, A. J.; Robbins, D. J.; Stewart, W. J. Magnetism from Conductors and Enhanced Nonlinear Phenomena. *IEEE Trans. Micro. Theory Technol.* **1999**, *47*, 2075−2084.

(6) Jaksic, Z.; Vukovic, S.; Matovic, J.; Tanaskovic, D. Negative Refractive Index Metasurfaces for Enhanced Biosensing. *Materials* **2011**, *4*, 1−36.

(7) Chen, T.; Li, S.; Sun, H. Metamaterials Application in Sensing. *Sensors* **2012**, *12*, 2742−2765.

(8) Xu, H.-X.; Wang, G.-M.; Mei, Q. Q.; Lv, Y.-Y.; Gao, X. Metamaterial Lens Made of Fully Printed Resonant-Type Negative-Refractive-Index Transmission Lines. *Appl. Phys. Lett.* **2013**, *102*, 193502.

(9) Schurig, D.; Mock, J. J.; Justice, B. J.; Cummer, S. A.; Pendry, J. B.; Starr, A. F.; Smith, D. R. Metamaterial Electromagnetic Cloak at Microwave Frequencies. *Science* **2006**, *314*, 977−980.

(10) Kante, B.; de Lustrac, A.; Lourtioz, J.-M.; Burokur, S. N. Infrared Cloaking Based on the Electric Response of Split Ring Resonators. *Opt. Express* **2008**, *16*, 9191−9198.

(11) Alici, K. B.; Turhan, A. B.; Soukoulis, C. M.; Ozbay, E. Optically Thin Composite Resonant Absorber at the Near-Infrared Band: a Polarization Independent and Spectrally Broadband Configuration. *Opt. Express* **2011**, *19*, 14260−14267.

(12) Watts, C. M.; Liu, X.; Padilla, W. J. Metamaterial Electromagnetic Wave Absorbers. *Adv. Mater.* **2012**, *24*, OP98−OP120.

(13) Xie, Q.; Hong, M. H.; Tan, H. L.; Chen, G. X.; Shi, L. P.; Chong, T. C. Fabrication of Nanostructures with Laser Interference Lithography. *J. Alloys Compd.* **2008**, *449*, 261−264.

(14) Lin, Y.; Hong, M. H.; Chong, T. C.; Lim, C. S.; Chen, G. X.; Tan, L. S.; Wang, Z. B.; Shi, L. P. Ultrafast-Laser-Induced Parallel Phase-Change Nanolithography. *Appl. Phys. Lett.* **2006**, *89*, 041108.

(15) Chen, Z.; Mohsen, R.; Gong, Y.; Chong, T. C.; Hong, M. Realization of Variable Three-Dimensional Terahertz Metamaterial Tubes for Passive Resonance Tunability. *Adv. Mater.* **2012**, *24*, OP143−OP147.

(16) Tang, Z.; Wei, A. Fabrication of Anisotropic Metal Nanostructures Using Innovations in Template-Assisted Lithography. *ACS Nano* **2012**, *6*, 998−1003.

(17) Shumaker-Parry, J. S.; Rochholz, H.; Kreiter, M. Fabrication of Crescent-Shaped Optical Antennas. *Adv. Mater.* **2005**, *17*, 2131−2134.

(18) Rochholz, H.; Bocchio, N.; Kreiter, M. Tuning Resonances on Crescent-Shaped Noble-Metal Nanoparticles. *New J. Phys.* **2007**, *9*, 1−18.

(19) Retsch, M.; Tamm, M.; Bocchio, N.; Horn, N.; Foerch, R.; Jonas, U.; Kreiter, M. Parallel Preparation of Densely Packed Arrays of 150 nm Gold-Nanocrescent Resonators in Three Dimensions. *Small* **2009**, *5*, 2105−2110.

(20) Wu, L. Y.; Ross, B. M.; Lee, L. P. Optical Properties of the Crescent-Shaped Nanohole Antenna. *Nano Lett.* **2009**, *9*, 1956−1961.

(21) Vogel, N.; Fischer, J.; Mohammadi, R.; Retsch, M.; Butt, H.-J.; Landfester, K.; Weiss, C. K.; Kreiter, M. Plasmon Hybridization in Stacked Double Crescents Arrays Fabricated by Colloidal Lithography. *Nano Lett.* **2011**, *11*, 446−454.

(22) Cataldo, S.; Zhao, J.; Neubrech, F.; Frank, B.; Zhang, C.; Braun, P. V.; Giessen, H. Hole-Mask Colloidal Nanolithography for Large-Area Low-Cost Metamaterials and Antenna-Assisted Surface-Enhanced Infrared Absorption Substrates. *ACS Nano* **2012**, *6*, 979−985.

(23) Xu, Q.; Bao, J.; Rioux, R. M.; Perez-Castillejos, R.; Capasso, F.; Whitesides, G. M. Fabrication of Large-Area Patterned Nanostructures for Optical Applications by Nanoskiving. *Nano Lett.* **2007**, *7*, 2800−2805.

(24) Lipomi, D. J.; Kats, M. A.; Kim, P.; Kang, S. H.; Aizenberg, J.; Capasso, F.; Whitesides, G. M. Fabrication and Replication of Arrays of Single- or Multicomponent Nanostructures by Replica Molding and Mechanical Sectioning. *ACS Nano* **2010**, *4*, 4017−4026.

(25) Gao, L.; Lin, L.; Hao, J.; Wang, W.; Ma, R.; Xu, H.; Yu, J.; Lu, N.; Wang, W.; Chi, L. Fabrication of Split-Ring Resonators by Tilted Nanoimprint Lithography. *J. Colloid Interface Sci.* **2011**, *360*, 320−323.

(26) Cai, Y.; Zhao, Z.; Chen, J.; Yang, T.; Cremer, P. S. Deflected Capillary Force Lithography. *ACS Nano* **2012**, *6*, 1548−1556.

(27) Cai, Y.; Li, Y.; Nordlander, P.; Cremer, P. S. Fabrication of Elliptical Nanorings with Highly Tunable and Multiple Plasmonic Resonances. *Nano Lett.* **2012**, *12*, 4881−4888.

(28) Johnson, P. B.; Christy, R. W. Optical Constants of the Noble Metals. *Phys. Rev. B* **1972**, *6*, 4370−4379.

(29) Bruinink, C. M.; Peter, M.; Maury, P. A.; de Boer, M.; Kuipers, L.; Huskens, J.; Reinhoudt, D. N. Capillary Force Lithography: Fabrication of Functional Polymer Templates as Versatile Tools for Nanolithography. *Adv. Funct. Mater.* **2006**, *16*, 1555−1565.

(30) Lee, S. Y.; Jeong, J.-R.; Kim, S.-H.; Kim, S.; Yang, S.-M. Arrays of Ferromagnetic Nanorings with Variable Thickness Fabricated by Capillary Force Lithography. *Langmuir* **2009**, *25*, 12535−12540.

(31) Zheng, Y. B.; Huang, T. J.; Desai, A. Y.; Wang, S. J.; Tan, L. K.; Gao, H.; Huan, A. C. H. Thermal Behavior of Localized Surface Plasmon Resonance of Au/TiO_2 Core/Shell Nanoparticle Arrays. *Appl. Phys. Lett.* **2007**, *90*, 183117.

(32) Zheng, Y. B.; Juluri, B. K.; Mao, X.; Walker, T. R.; Huang, T. J. Systematic Investigation of Localized Surface Plasmon Resonance of Long-Range Ordered Au Nanodisk Arrays. *J. Appl. Phys.* **2008**, *103*, 014308.

(33) Yang, S.; Xu, F.; Ostendorp, S.; Wilde, G.; Zhao, H.; Lei, Y. Template-Confined Dewetting Process to Surface Nanopatterns: Fabrication, Structural Tunability, and Structure-Related Properties. *Adv. Funct. Mater.* **2011**, *21*, 2446−2455.

(34) Bocchio, N. L.; Unger, A.; Alvarez, M.; Kreiter, M. Thin Layer Sensing with Multipolar Plasmonic Resonances. *J. Phys. Chem. C* **2008**, *112*, 14355−14359.

(35) Chen, C.-Y.; Wu, S.-C.; Yen, T.-J. Experimental Verification of Standing-Wave Plasmonic Resonances in Split-Ring Resonators. *Appl. Phys. Lett.* **2008**, *93*, 034110.

(36) Nordlander, P. The Ring: a Leitmotif in Plasmonics. *ACS Nano* **2009**, *3*, 488−492.
(37) Neubrech, F.; Kolb, T.; Lovrincic, R.; Fahsold, G.; Pucci, A.; Aizpurua, J.; Cornelius, T. W.; Toimil-Molares, M. E.; Neumann, R.; Karim, S. Resonances of Individual Metal Nanowires in the Infrared. *Appl. Phys. Lett.* **2006**, *89*, 253104.